SPE 89428

Physically-Based Capillary Pressure Correlation For Mixed-Wet Reservoirs From A Bundle-Of-Tubes Model

J.O. Helland, SPE, and S.M. Skjæveland, SPE, University of Stavanger

Copyright 2004, Society of Petroleum Engineers Inc.

This paper was prepared for presentation at the 2004 SPE/DOE Fourteenth Symposium on Improved Oil Recovery held in Tulsa, Oklahoma, U. S. A., 17–21 April 2004.

This paper was selected for presentation by an SPE Program Committee following review of information contained in a proposal submitted by the author(s). Contents of the paper, as presented, have not been reviewed by the Society of Petroleum Engineers and are subject to correction by the author(s). The material, as presented, does not necessarily reflect any position of the Society of Petroleum Engineers, its officers, or members. Papers presented at SPE meetings are subject to publication review by Editorial Committees of the Society of Petroleum Engineers. Electronic reproduction, distribution, or storage of any part of this paper for commercial purposes without the written consent of the Society of Petroleum Engineers is prohibited. Permission to reproduce in print is restricted to a proposal of not more than 300 words; illustrations may not be copied. The proposal must contain conspicuous acknowledgment of where and by whom the paper was presented. Write Librarian, SPE, P.O. Box 833836, Richardson, TX 75083-3836, U.S.A., fax 01-972-952-9435.

Abstract

It is shown that the main characteristics of mixed-wet capillary pressure curves with hysteretic scanning loops can be reproduced by a bundle-of-triangular-tubes model. Accurate expressions for the entry pressures are employed, truly accounting for the mixed wettability and the diverse fluid configurations that arise from contact angle hysteresis and pore shape. The simulated curves are compared with published correlations that have been suggested by inspection of laboratory data from core plug experiments.

Introduction

Knowledge of the functional relationship between capillary pressure and saturation is required in numerical models to solve the equations for fluid flow in the reservoir. In practice, this relationship is formulated as a capillary pressure correlation with several parameters that usually are to be determined from experimental data. Generally it is not evident how these parameters should be adjusted to account for variations in physical properties like wettability, pore shape, pore-size distribution, and the underlying pore-scale processes. Hence, a more physically-based correlation, accounting for observable properties, would improve the reliability of the correlation and extend its applicability range.

Among the correlations reported in the litterature, the Brooks-Corey formula is one of the most frequently used because of its simplicity and solid experimental validation.[1] This correlation may be written as

$$P_c = cS_w^{-a}, \qquad (1)$$

where c is the entry pressure, $1/a$ the pore-size distribution index, and S_w the normalized water saturation. Skjaeveland *et al.*[2] extended the correlation to account for imbibition, secondary drainage and hysteresis scanning loops for mixed-wet conditions, resulting in the expression

$$P_c = c_w S_w^{-a_w} + c_o S_o^{-a_o}, \qquad (2)$$

where S_o is the normalized oil saturation. In general, Eq. 2 requires different sets of the constants a_w, a_o, c_w and c_o for different drainage and imbibition capillary pressure curves. Hence, a systematic method based on physical principles to determine the sets of parameters is advisable, as this would increase the reliability of Eq. 2 in practical applications.

Analytical correlations may be derived assuming a bundle-of-tubes representation of the pore network. Following this approach for a model of cylindrical tubes, Huang *et al.*[3] derived a capillary pressure correlation for primary drainage and the hysteresis bounding loop, accounting for variations in wettability. Princen[4] computed numerically the relationship between capillary pressure and saturation for primary drainage and imbibition for a bundle of tubes with curved triangular cross-sections of uniform wettability. He made no attempt, however, to develop any correlation.

We have chosen to generate artificial capillary pressure curves from a simple simulation model, and then compare the simulation results to Eqs. 1, 2 with estimated parameters. We assume that the pore network is represented by a bundle-of-tubes model, the tubes having triangular, equilateral, cross-sections. Such a representation is simplistic, as it does not account for the interconnectivity of real porous media and the converging-diverging nature of pore throats. Thus, the mechanisms leading to phase entrapment and residual saturations are absent in our model, and hence contact angle hysteresis is the only factor that leads to hysteresis between imbibition and drainage capillary pressure curves. However, the triangular cross-sectional shape allows for representation of other important physical processes such as the development of mixed wettability within a single pore[5,6] and oil drainage through layers in the crevices.[7–9] Simple models that account for important physical properties are invaluable as they allow for careful interpretation of the simulated results and also make it possible to derive analytical expressions between key parameters that describe general trends in measured data. This, in turn, can be used to suggest reliable physically-based correlations. Such a methodology may not be expedient by use of sophisticated pore-scale network models because of the complex description of the pore space.[10,11] Hui and Blunt[9] studied trends in two- and three-phase relative permeabilities using a bundle of triangular tubes. Our model is programmed in MATLAB[†] and generates capillary pressure curves for primary drainage with wettability alteration, imbibition and secondary drainage with provisions for hysteresis loops from any reversal point. This sequence of processes leads to a diversity of cross-sectional fluid configurations due to the angular pore shape and contact angle hysteresis.

The objective of this paper is twofold. First we demonstrate that the model reproduces the main characteristics of realistic capillary pressure curves with hysteretic scanning loops for mixed-wet conditions. Second we derive algebraic expressions that correlate saturation and capillary pressure. The simulated curves are finally compared with Eqs. 1, 2.

Model Description

The pore network is represented as a bundle of parallel tubes, the tubes having equilateral, triangular cross-sections. The geometry of an equilateral triangle is readily described by the half-angle of the corner, $\alpha = \frac{\pi}{6}$, and the radius of the inscribed circle R. The pore-size frequency is described by a truncated two-parameter Weibull distribution[12] which we believe is adequate for characterizations of a wide range of core samples. For convenience, we take R as the distributed parameter. The density is then given by

$$f(R) = \frac{\left[\frac{R-R_{\text{min}}}{R_{\text{ch}}}\right]^{\eta-1} \frac{\eta}{R_{\text{ch}}} \exp(-\left[\frac{R-R_{\text{min}}}{R_{\text{ch}}}\right]^{\eta})}{1-\exp(-\left[\frac{R_{\text{max}}-R_{\text{min}}}{R_{\text{ch}}}\right]^{\eta})}, \qquad (3)$$

where R_{max}, R_{min} and R_{ch} are the inscribed radii of the largest, smallest and characteristic pore sizes, respectively, and η is a dimensionless parameter. The pore sizes in the model are selected from the corresponding cumulative distribution function in the following manner: Pick random numbers $x \in [0, 1]$ and calculate the the inscribed radius from

$$R = R_{\text{ch}}\Big(-\ln[(1-x)\exp(-\left[\frac{R_{\text{max}}-R_{\text{min}}}{R_{\text{ch}}}\right]^{\eta}) + x]\Big)^{\frac{1}{\eta}} + R_{\text{min}}. \quad \ldots \quad (4)$$

The cross-sectional area A is then related to R by

$$A = \frac{3R^2}{\tan\alpha}. \quad \ldots \quad (5)$$

An invasion process is simulated by increasing or decreasing the capillary pressure stepwise until some maximum or minimum value is reached. At each step the tubes are tested for invasion and the saturation is calculated.

The capillary entry pressures are calculated by the MS-P method named after the contributions from Mayer and Stowe [13] and Princen.[14–16] This method is founded on an energy balance equation which equates the virtual work with the associated change of surface free energy for a small displacement of the interface in the direction along the tube. The energy balance equation then relates the entry radius of curvature to the cross-sectional area exposed to change of fluid occupancy, the bounding cross-sectional fluid-solid and fluid-fluid lengths, and the contact angle. Following this approach, Ma *et al.*[17] derived the entry pressures for primary drainage and imbibition for mixed-wet triangular pores.

There are generally two scenarios that need to be considered separately depending on the contact angle θ. As an example, consider oil invasion into a uniformly wetted tube initially filled with water. If

$$\theta < \frac{\pi}{2} - \alpha, \quad \ldots \quad (6)$$

oil invasion results in a cross-sectional fluid configuration where oil has occupied the bulk area while water is still residing in the corners. If the contact angle does not satisfy Eq. 6, oil occupies the entire tube during invasion. The invading interface separating the bulk fluids is referred to as the main terminal meniscus (MTM), and the interface separating bulk fluid from corner fluid is referred to as the arc meniscus (AM). The curvature of an AM is represented by a cross-sectional circular arc of radius r. Hence, the applied capillary pressure may be expressed as

$$P_c = \frac{\sigma}{r}, \quad \ldots \quad (7)$$

where σ is the interfacial tension.

The total area of fluid residing in the corners of a tube after invasion is given by

$$A_c(\theta) = 3r^2(\theta + \alpha - \frac{\pi}{2} + \cos\theta(\frac{\cos\theta}{\tan\alpha} - \sin\theta)). \quad . \quad (8)$$

Combinations of Eqs. 5, 8 provide the expressions employed in the saturation calculations, accounting for all fluid configurations.

We simulate primary drainage with wettability alteration, imbibition and secondary drainage with provisions for hysteresis loops from arbitrary reversal points. The different cross-sectional fluid configurations that may arise during the simulations are depicted in **Fig. 1**. Configuration A shows a tube that always has been waterfilled. The configurations B–F represent tubes that at some point have been invaded by oil. The areas where oil has contacted the pore walls, marked by the bold lines, have altered wettability.

We assume that any effects of wetting films[18] and surface roughness[19] is included in the combination of the contact angles used, as a more detailed description of these properties would require knowledge of the mineralogy and geometry of the pore surface in addition to molecular properties. We believe that this is a reasonable assumption since the saturation-contribution to wetting films is neglible, and, with the present representation of the pore network, no qualitative difference in capillary behavior is expected.

Primary Drainage. All tubes are waterfilled and strongly waterwet initially, and hence we assume that the contact angle during primary drainage, θ_{pd}, always is small and satisfies Eq. 6. Oil invasion is then a displacement from configuration A in

---

[†] MATLAB is a registered trademark of TheMathWorks Inc.

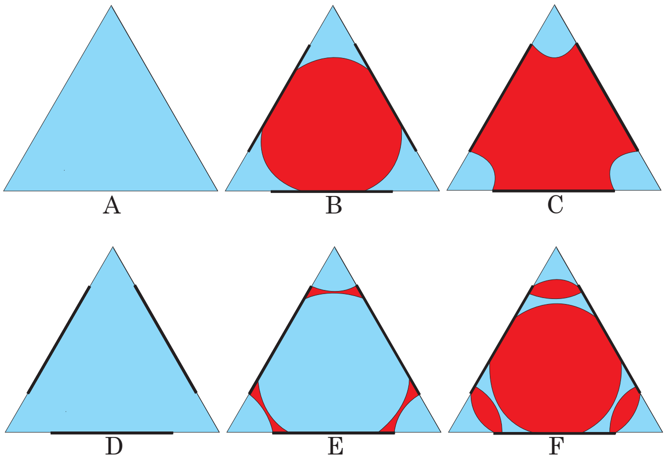

Figure 1: Fluid configurations for primary drainage, imbibition, and secondary drainage, with water in light blue, and oil in dark red. The bold lines along the sides indicate altered wettability.

Fig. 1 to the configuration shown in **Fig. 2**. The capillary entry pressure for this event is given by

$$P_c = \frac{\sigma}{R}\left[\cos\theta_{pd} + \sqrt{\frac{\tan\alpha}{2}(\sin 2\theta_{pd} - 2\theta_{pd} - 2\alpha + \pi)}\right]. \tag{9}$$

As primary drainage proceeds, oil invades successively smaller tubes, whereas the water content in the corners of the invaded tubes is reduced according to Eq. 7. We assume that oil always contacts the pore walls, leaving the sides wettability-altered and the corners waterwet after terminated primary drainage. The length b_{pd} of the solid surface that remains waterwet is

$$b_{pd} = \frac{\sigma\cos(\theta_{pd} + \alpha)}{P_c^{\max}\sin\alpha}. \tag{10}$$

The $P_c^{\max}$ - value and the corresponding water saturation is the reversal point on the primary drainage curve. According to Eq. 10, the area of the waterwet surface is the same for all tubes invaded by oil during primary drainage. Thus the smaller tubes have the largest fraction of waterwet surface and should therefore exhibit a more waterwet behavior than the larger ones during imbibition.

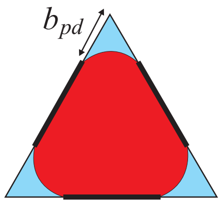

Figure 2: Final configuration of a tube after primary drainage. The bold lines along the sides represent the lengths of the pore wall with altered wettability. The distances b_{pd} in the corners remain waterwet.

Imbibition. The amount of contact angle hysteresis between primary drainage and imbibition depends on the degree of wettability alteration and surface roughness.[19,20] To study different wetting conditions we allow all advancing contact angles θ_a measured on the wettability-altered surface, that satisfies $\theta_a \geq \theta_{pd}$.

Pore filling during waterflooding may in general occur by two different mechanisms: Piston-like displacement (invasion of an MTM) and snap-off (coalescence of the AMs as a result of increased water content in the corners). Even though the model is programmed to check for snap-off events, we find that piston-like invasion always is the favorable displacement type. For a description of the snap-off equations we refer to Hui and Blunt.[9] They comment that snap-off may only occur in network representations of the pore space when piston-like displacement is impossible.

As the capillary pressure decreases from $P_c^{\max}$, the AMs are hinging at position b_{pd} with the hinging contact angle θ_h increasing from θ_{pd} towards θ_a according to

$$\theta_h = \cos^{-1}\left[\frac{P_c b_{pd}\sin\alpha}{\sigma}\right] - \alpha. \tag{11}$$

If θ_a satisfies Eq. 6, the hinging contact angle may reach θ_a before invasion of an MTM. In this case the AMs are free to move with contact angle θ_a on the surface of altered wettability, and configuration B is attained. If θ_a does not satisfy Eq. 6, the AMs are still hinging, and the tubes assume configuration C.

Along with the increase of water content in the corners during imbibition, piston-like invasion must be considered for both configuration B and C. When configuration B occurs for the first time during imbibition, Eq. 6 is always satisfied, and hence invasion of an MTM is a spontaneous displacement from configuration B to D. The entry pressure is given by

$$P_c = \frac{\sigma}{R}\left[\cos\theta_a + \sqrt{\frac{\tan\alpha}{2}(\sin 2\theta_a - 2\theta_a - 2\alpha + \pi)}\right]. \tag{12}$$

For invasion into tubes of configuration C there are two different expressions for the capillary entry pressure. If $\theta_a \leq \frac{\pi}{2} + \alpha$, the displacement is always from configuration C to D. In this case the hinging contact angle differs from the advancing contact angle, and the entry pressure must be calculated numerically. From the energy balance, equating the virtual work with the change of surface free energy for a small displacement of the MTM, the entry radius of curvature may be expressed as

$$r = \frac{A_{\text{eff}}}{L_s\cos\theta_a + L_f}, \tag{13}$$

where

$$A_{\text{eff}} = \frac{R^2}{2\tan\alpha} - \frac{r\,b_{pd}\sin(\alpha+\beta)}{2} + \frac{r^2\beta}{2}, \tag{14}$$

$$L_s = \frac{R}{\tan\alpha} - b_{pd}, \tag{15}$$

$$L_f = r\beta, \tag{16}$$

$$r\sin\beta = b_{pd}\sin\alpha, \tag{17}$$

with β defined as

$$\beta = \frac{\pi}{2} - \alpha - \theta_h. \qquad (18)$$

Eqs. 13–17 are iteratively solved to find r, and the capillary entry pressure is finally obtained from Eq. 7.

The displacement from configuration C to D may be spontaneous or forced. The limiting condition for spontaneous imbibition is zero capillary pressure, and hence the AMs are flat. From Eq. 13 this condition is

$$L_s \cos\theta_a + L_f = 0, \qquad (19)$$

with $L_f = b_{pd} \sin\alpha$. From Eq. 19 the advancing contact angle corresponding to zero capillary entry pressure is[17]

$$\theta_a^{\text{crit}} = \cos^{-1}\left[\frac{-b_{pd}\sin\alpha}{\frac{R}{\tan\alpha} - b_{pd}}\right]. \qquad (20)$$

Notice that the value of θ_a^{crit} depends on the reversal point from primary drainage since b_{pd} is a function of $P_c^{\max}$, according to Eq. 10. Since the corners are waterwet, the critical contact angle is always larger than $\frac{\pi}{2}$. If Eq. 19 instead is solved for R to find the pore size corresponding to zero capillary pressure, we find that

$$R = b_{pd} \tan\alpha \left(1 - \frac{\sin\alpha}{\cos\theta_a}\right), \qquad (21)$$

and hence R increases linearly with b_{pd} provided $\theta_a > \frac{\pi}{2}$. By Eqs. 20, 21, the triangular tube model induces a relation between wettability and reversal point from primary drainage. This is in agreement with the observation made by Jerauld and Rathmell[21] that reservoir wettability may be correlated with irreducible water saturation.

When the displacement from configuration C to D is enforced, the simple Young-Laplace equation has previously been used to estimate the capillary entry pressures.[9,10,22] However, this simple expression does not incorporate the wettability variation with pore size as a result of the amount of water residing in the corners after primary drainage. In **Fig. 3** the capillary entry pressure obtained from Eqs. 7, 13–17 is presented as a function of pore size for several values of $P_c^{\max}$ when $\theta_a = 110°$, $\theta_{pd} = 0°$ and $\sigma = 0.050$ N/m. As expected, the smaller tubes show a more waterwet behavior than the larger ones due to a larger fraction of waterwet surface. At negative capillary pressures, the invasion order depends on both wettability and pore size. **Fig. 3** also demonstrates that the tubes become more oilwet as $P_c^{\max}$ increases.

Finally we consider invasion of an MTM when $\theta_a > \frac{\pi}{2} + \alpha$. In this case oil layers may form between water in the corners and the bulk portion, and the displacement is from configuration C to E at a capillary entry pressure given by

$$P_c = \frac{\sigma}{R}\left[\cos\theta_a - \sqrt{\frac{\tan\alpha}{2}(-\sin 2\theta_a + 2\theta_a - 2\alpha - \pi)}\right]. (22)$$

According to van Dijke and Sorbie[23] and Helland,[24] water displaces the oil layers in configuration E in a piston-like displacement before the AMs surrounding the oil layers meet at their midpoints. This displacement is illustrated in **Fig. 4**, and the corresponding energy balance equation may be written as

$$\frac{A_{\text{eff}}}{r} = (L_{s1} - L_{s2})\cos\theta_a + L_{f1} + L_{f2}, \qquad (23)$$

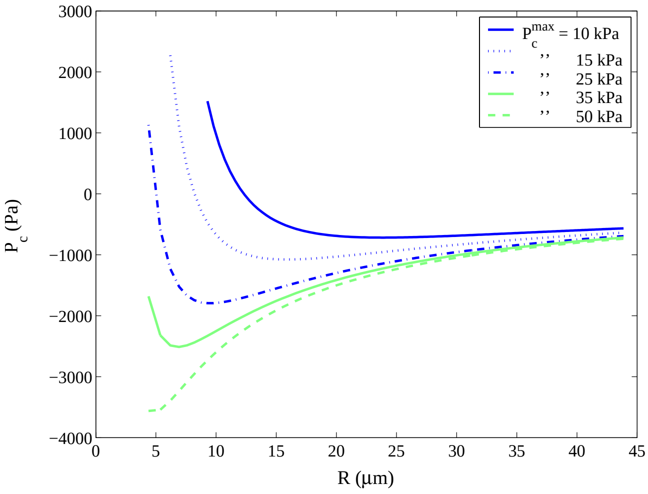

Figure 3: Capillary entry pressures as a function of pore size R for a displacement from configuration C to D when $\theta_a = 110°$.

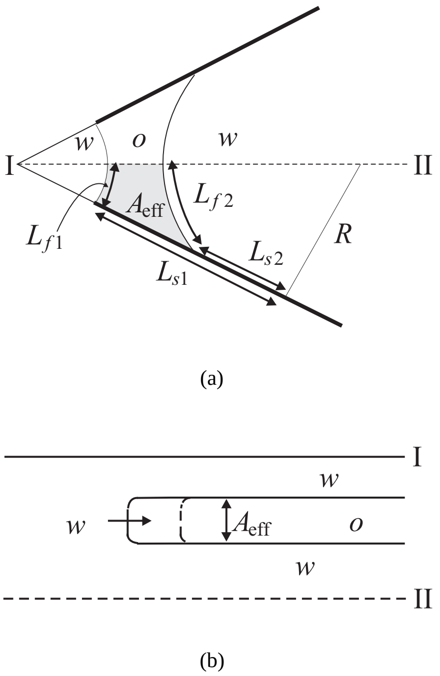

Figure 4: Representation of the cross-sectional parameters employed in the calculation of the capillary *layer* entry pressure. (a) Cross-sectional view of configuration E. (b) View of the displacement from configuration E to D in the direction along the tube length.

where

$$A_{\text{eff}} = \frac{r}{2}\{b\cos\theta_a - b_{pd}\cos\theta_h + r(\pi - \theta_a - \theta_h)\}, \tag{24}$$

$$L_{s1} - L_{s2} = b - b_{pd}, \tag{25}$$

and

$$L_{f1} + L_{f2} = r(\pi - \theta_h - \theta_a). \tag{26}$$

The distance b_{pd} remains fixed as θ_h changes with r, while the distance b changes with r at constant contact angle θ_a. These distances are eliminated from the equations using the relations

$$b = \frac{r\cos(\theta_a - \alpha)}{\sin\alpha}, \tag{27}$$

and

$$b_{pd} = \frac{r\cos(\theta_h + \alpha)}{\sin\alpha}. \tag{28}$$

Inserting Eqs. 24–28 into Eq. 23 yields

$$\begin{aligned}&\pi - \theta_a - \theta_h + \cos\theta_a\frac{\cos(\theta_a - \alpha)}{\sin\alpha} + \\ &(\cos\theta_h - 2\cos\theta_a)\frac{\cos(\theta_h + \alpha)}{\sin\alpha} = 0.\end{aligned} \tag{29}$$

Eq. 29 is solved for θ_h by iterations, using $\theta_h = \theta_a$ as initial value. The converged value of θ_h is used to calculate the capillary layer entry pressure P_c^l by combining Eqs. 7, 28.

Formation of oil layers may not be possible if the water content in the corners of configuration C is large. In that case a direct displacement from configuration C to D occurs. This situation is treated as follows: Assume that the displacement is from configuration C to E and calculate the capillary entry pressure from Eq. 22 and the layer entry pressure from Eq. 29 together with Eqs. 7, 28. If $P_c \leq P_c^l$, oil layer formation does not occur, and the entry pressure is again calculated from Eqs. 7, 13–17, assuming that the water invasion is a direct displacement from configuration C to D.

Secondary Drainage. Because of contact angle hysteresis, we allow all receding contact angles θ_r in secondary drainage that satisfies $\theta_{pd} \leq \theta_r \leq \theta_a$. To study saturation reversals from any point on the imbibition capillary pressure curve, we have to consider the configurations A–E separately. Any AMs located on the wettability-altered surface after imbibition are assumed to be hinging at their positions while the contact angle decreases from θ_a towards θ_r with increased capillary pressure.

The tubes remaining at configuration A are strongly waterwet and assigned the same contact angle as in primary drainage, i.e., θ_{pd}. Oil invasion occurs when the secondary drainage curve reaches the first reversal point on the primary drainage curve, i.e., when $P_c \geq P_c^{\max}$. Then oil invasion is a displacement from configuration A to the configuration shown in **Fig. 2** at a capillary entry pressure given by Eq. 9. A previously waterflooded tube attains a configuration shown in **Fig. 2** when $P_c = P_c^{\max}$. This ensures that the imbibition and secondary drainage curves constitute a closed hysteresis loop. During further increments of the capillary pressure, the AMs move towards the corners with contact angle θ_{pd}, and the length of waterwet surface, b_{pd}, decreases.

In configuration B and C oil occupies the bulk area, and hence invasion of MTMs does not occur. In configuration C the AMs are hinging at position b_{pd} while the contact angle decreases with increasing capillary pressure according to Eq. 11. When $P_c = P_c^{\max}$, the contact angle has decreased to θ_{pd} and the AMs are free to move towards the corners during further capillary pressure increments. In configuration B the AMs are stuck at position b_{imb} corresponding to the capillary pressure $P_c^{\min}$ at which the imbibition was terminated,

$$b_{\text{imb}} = \frac{\sigma\cos(\theta_a + \alpha)}{P_c^{\min}\sin\alpha}. \tag{30}$$

The AMs are hinging while the contact angle decreases from θ_a to θ_r according to

$$\theta_h = \cos^{-1}\left[\frac{P_c b_{\text{imb}}\sin\alpha}{\sigma}\right] - \alpha. \tag{31}$$

When $\theta_h = \theta_r$, the AMs move towards position b_{pd} with increasing capillary pressure, and eventually configuration C is reached.

For piston-like oil invasion into tubes of configuration D, there are three different expressions for the entry pressure depending on the displacement type and contact angle. If $\theta_r < \frac{\pi}{2} - \alpha$, the displacement is either from configuration D to B or from D to C. We consider from D to B, first. The capillary entry pressure is then calculated from

$$P_c = \frac{\sigma}{R}\left[\cos\theta_r + \sqrt{\frac{\tan\alpha}{2}(\sin 2\theta_r - 2\theta_r - 2\alpha + \pi)}\right], \tag{32}$$

and the corresponding position b of the invading AMs for the associated displacement is

$$b = \frac{\sigma\cos(\theta_r + \alpha)}{P_c\sin\alpha}. \tag{33}$$

If $b > b_{pd}$, the displacement is indeed from configuration D to B, and the capillary entry pressure is given by Eq. 32. If $b \leq b_{pd}$, the displacement is from configuration D to C, and the correct entry pressure is calculated numerically as for the reversed displacement during imbibition. The equivalent of Eq. 13 is

$$r = \frac{A_{\text{eff}}}{L_s\cos\theta_r + L_f}. \tag{34}$$

Eqs. 14–17, 34 provide the set of equations to be solved iteratively for r. The capillary entry pressure is finally calculated from Eq. 7.

If $\frac{\pi}{2} - \alpha \leq \theta_r \leq \frac{\pi}{2} + \alpha$, the displacement is always from configuration D to C, and the capillary entry pressure is again calculated from Eqs. 7, 14–17, 34.

If $\theta_r > \frac{\pi}{2} + \alpha$, oil invasion into configuration D is either a displacement to configuration C, or, if oil enters as layers, to configuration E. The equivalent of Eq. 29 for the oil layer invasion is

$$\begin{aligned}&\pi-\theta_r-\theta_h+\cos\theta_r\frac{\cos(\theta_r-\alpha)}{\sin\alpha}+\\&(\cos\theta_h-2\cos\theta_r)\frac{\cos(\theta_h+\alpha)}{\sin\alpha}=0.\end{aligned} \quad \ldots\ldots \quad (35)$$

Eq. 35 is solved iteratively for θ_h with $\theta_h=\theta_r$ as initial value. The layer entry pressure P_c^l for the displacement from configuration D to E is finally calculated from Eqs. 7, 28. To determine the actual displacement occuring, we also calculate the capillary entry pressure P_c for the displacement from configuration D to C by Eqs. 7, 14–17, 34. If $P_c \le P_c^l$, oil layers do not form and the displacement is indeed from configuration D to C. If $P_c > P_c^l$, the displacement from configuration D to E occurs instead.

Finally we consider configuration E. After terminated imbibition the innermost AMs (separating oil from bulk water) are located at position

$$b_{\mathrm{imb}}=\frac{\sigma\cos(\theta_a-\alpha)}{P_c^{\min}\sin\alpha}. \quad \ldots\ldots \quad (36)$$

As the capillary pressure increases, the hinging contact angle decreases from θ_a towards θ_r according to

$$\theta_h=\cos^{-1}\left[\frac{P_c b_{\mathrm{imb}}\sin\alpha}{\sigma}\right]+\alpha. \quad \ldots\ldots \quad (37)$$

At the same time, the corner AMs (separating oil from water in the corners) are stuck at position b_{pd}, with the contact angle varying according to Eq. 11. These events lead to a swelling of the oil layers. If $\theta_r > \frac{\pi}{2}+\alpha$, the innermost AMs may begin to move away from the corners at a negative capillary pressure when the contact angle has reached θ_r.

For MTM invasion into configuration E, there are three expressions for the capillary entry pressures. If $\theta_r > \frac{\pi}{2}+\alpha$, the displacement is from configuration E to C, and the entry pressure is given by

$$P_c=\frac{\sigma}{R}\left[\cos\theta_r-\sqrt{\frac{\tan\alpha}{2}(-\sin 2\theta_r+2\theta_r-2\alpha-\pi)}\right]. \quad (38)$$

Eq. 38 is exact when the contact angle of the innermost AMs has reached θ_r before invasion, and approximate otherwise.

If $\frac{\pi}{2}-\alpha \le \theta_r \le \frac{\pi}{2}+\alpha$, the displacement is still from configuration E to C. In this case the innermost AMs do not move before invasion, and the capillary entry pressure is again calculated numerically. The entry radius of curvature is now given by

$$r=\frac{A_{\mathrm{eff}}}{L_s\cos\theta_r-L_f}, \quad \ldots\ldots \quad (39)$$

where

$$A_{\mathrm{eff}}=\frac{R^2}{2\tan\alpha}-\frac{r b_{\mathrm{imb}}\sin(\beta-\alpha)}{2}-\frac{r^2\beta}{2}, \quad \ldots\ldots \quad (40)$$

$$L_s=\frac{R}{\tan\alpha}-b_{\mathrm{imb}}, \quad \ldots\ldots \quad (41)$$

$$L_f=r\beta, \quad \ldots\ldots \quad (42)$$

$$r\sin\beta=b_{\mathrm{imb}}\sin\alpha, \quad \ldots\ldots \quad (43)$$

with β defined as

$$\beta=\frac{\pi}{2}+\alpha-\theta_h. \quad \ldots\ldots \quad (44)$$

The parameters b_{imb} and θ_h are given by Eq. 36, 37, respectively. Eqs. 39–43 are solved by iterations, and the capillary entry pressure is finally obtained from Eq. 7.

If $\theta_r < \frac{\pi}{2}-\alpha$, invasion of an MTM may result in formation of water layers surrounded by bulk oil and oil in layers. In this case the displacement is from configuration E to F, at a capillary entry pressure given by Eq. 32. Oil displaces the water layers in configuration F in a piston-like displacement before the surrounding AMs meet at their midpoints. The energy balance equation for this event yields

$$\begin{aligned}&\pi-\theta_r-\theta_h-\cos\theta_r\frac{\cos(\theta_r+\alpha)}{\sin\alpha}-\\&(\cos\theta_h-2\cos\theta_r)\frac{\cos(\theta_h-\alpha)}{\sin\alpha}=0,\end{aligned} \quad \ldots\ldots \quad (45)$$

which is derived in the same manner as Eq. 29. Eq. 45 is solved for θ_h which now represents the hinging contact angle of the AM separating the water and oil layers. The layer entry pressure is finally calculated by

$$P_c^l=\frac{\sigma\cos(\theta_h-\alpha)}{b_{\mathrm{imb}}\sin\alpha}, \quad \ldots\ldots \quad (46)$$

and the displacement is from F to C.

Formation of water layers may not be possible if the distance b_{imb} in configuration E is large, indicating a direct displacement from configuration E to C. This situation is treated in the same way as for the oil layers during imbibition: Assume a displacement from configuration E to F and calculate the corresponding entry pressure from Eq. 32 and the layer entry pressure from Eqs. 45, 46. If $P_c \ge P_c^l$, water layers do not form, and the entry pressure is again calculated from Eqs. 7, 39–43, assuming a direct displacement from configuration E to C.

The displacements from configuration D to C and from E to C may be spontaneous or forced. As opposed to waterflooding, oil invasion is a spontaneous process when the receding contact angle is larger than some value θ_r^{crit} corresponding to zero capillary pressure. For the displacement from configuration D to C the critical contact angle is given by Eq. 20. The displacement from configuration E to C exhibits a somewhat different capillary behavior due to the existence of oil layers in configuration E. In this case the equivalent of Eq. 20 is derived from Eq. 39 resulting in the expression

$$\theta_r^{\mathrm{crit}}=\cos^{-1}\left[\frac{b_{\mathrm{imb}}\sin\alpha}{\frac{R}{\tan\alpha}-b_{\mathrm{imb}}}\right]. \quad \ldots\ldots \quad (47)$$

Notice that θ_r^{crit} depends on the reversal point from imbibition since b_{imb} is a function of $P_c^{\min}$. The bulk water in configuration E is bounded by oil layers in the corners, and hence the critical contact angle is always smaller than $\frac{\pi}{2}$. In **Fig. 5** the capillary entry pressure estimated from Eqs. 39–43 is presented as a function of pore size for several values of $P_c^{\min}$ when $P_c^{\max} = 50$ kPa, $\theta_{pd} = 0°$, $\theta_a = 180°$, $\theta_r = 70°$ and $\sigma = 0.050$ N/m. In this case the capillary entry pressure is increasingly affected by the oil layers with decreasing pore size, and hence the smaller tubes exhibit a more oilwet behavior than the larger ones in the sense of decreased entry pressures. When $P_c^{\min}$ decreases, the innermost AMs in configuration E move towards the corners and the effect of the oil layers on the drainage entry pressure is reduced resulting in a less oilwet behavior.

The capillary behavior illustrated by **Figs. 3, 5** indicates that the wettability of angular pore shapes may not be appropriately described by the contact angle measured on the surface of altered wettability. A macroscopic measure based on interpretations of the capillary pressure curves seems more plausible.

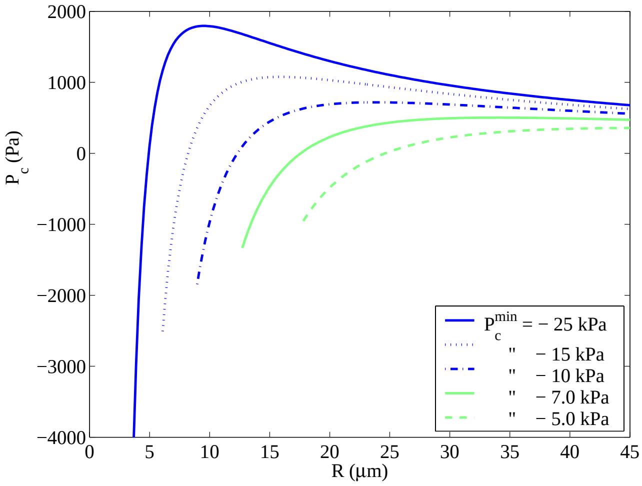

Figure 5: Capillary entry pressures as a function of pore size R for a displacement from configuration E to C when $\theta_r = 70°$.

Additional Saturation Reversals. To account for subsequent saturation reversals it is assumed that new fluid configurations do not arise during the processes following secondary drainage. When configuration B arises for the first time in secondary drainage it is possible that oil layers may form during the subsequent imbibition process. However, in this case we always assume that water invasion is a displacement from configuration B to D for any value of θ_a. We believe this is a reasonable simplification since the high water content in the corners of configuration B makes oil layer formation less likely. If θ_a satisfies Eq. 6, the capillary entry pressure for this displacement is calculated from Eq. 12. This expression is accurate when the hinging contact angle of the AMs has reached θ_a before the MTM invasion, and is used as an approximation otherwise. If Eq. 6 is not satisfied, the capillary entry pressure is calculated from Eqs. 7, 13–17 with b_{pd} replaced by the updated positions of the AMs after terminated secondary drainage. Similarly, a water invasion into tubes of configuration F is always assumed to displace all of the bulk oil, resulting in a displacement from configuration F to E. The capillary entry pressure for this displacement is calculated from Eqs. 7, 13–17 with b_{pd} replaced by the updated positions of the innermost AMs in configuration F at the end of the secondary drainage process. Notice also that the displacement from configuration F to C in secondary drainage can not occur in the reversed direction during imbibition. This is caused by the large contact angle hysteresis required for the existence of configuration F, i.e., $\theta_a > \frac{\pi}{2} + \alpha$ and $\theta_r < \frac{\pi}{2} - \alpha$, which makes such a displacement geometrically impossible.

With the simplified treatment of configuration B and F during secondary imbibition the model provides for scanning hysteresis loops starting from any reversal point. In all cases an invasion event is a displacement between two of the configurations A–F. At each capillary pressure step the hinging contact angles of the stuck AMs and the positions b of the moving AMs are calculated. The imbibition entry pressures are updated before each imbibition process, and the drainage entry pressures are updated before each drainage process.

Simulation Results. We have performed simulations of capillary pressure curves for a bundle of 2000 tubes. The pore sizes are calculated from Eq. 4 assuming $R_{\text{min}} = 0.1\mu$m, $R_{\text{max}} = 100\mu$m, $R_{\text{ch}} = 20\mu$m and $\eta = 1.5$. In all experiments we let $\theta_{pd} = 0°$, reflecting displacements on water-coated surfaces during primary drainage. The interfacial tension employed is $\sigma = 0.050$ N/m. For the sample of results presented here, primary drainage is always terminated at a $P_c^{\max}$ - value at which some of the smallest tubes remain waterfilled. This value is chosen arbitrarily since the model does not allow for residual saturations due to phase entrapment. The corresponding value of S_w serves as an initial water saturation S_{wi}.

Fig. 6 illustrates the effect of the advancing contact angle on the imbibition curve. When $\theta_a = 100°$, the displacement is from configuration C to D, and the effect of the waterfilled corners on the entry pressure decreases with increasing pore size, as demonstrated by **Fig. 3**. This produces a large, almost horizontal, segment on the imbibition curve with a smooth transition from positive to negative capillary pressure. When $\theta_a = 140°$, water first invades a few of the larger tubes in a displacement from configuration C to E followed by the displacement from configuration E to D. When the larger tubes have reached their final configuration D, water invasion proceeds in the smaller tubes by direct displacements from configuration C to D, still with the entry pressures heightened by the water content residing in the corners, as demonstrated by **Fig. 3**. This behavior is also observed when $\theta_a = 180°$, even though the displacement from configuration C to E is predominant.

Fig. 7 shows imbibition curves originating at different reversal points from primary drainage when $\theta_a = 180°$. At low $P_c^{\max}$ - values the displacement is primarily from configuration C to D due to a considerable water content in the corners. An increased $P_c^{\max}$ reduces this water content, and the displacement from configuration C to E becomes predominant. The saturation change caused by the hinging AMs during imbibition is conspicuous for intermediate $P_c^{\max}$ - values as the contribution to the water saturation from tubes of configuration C is at a

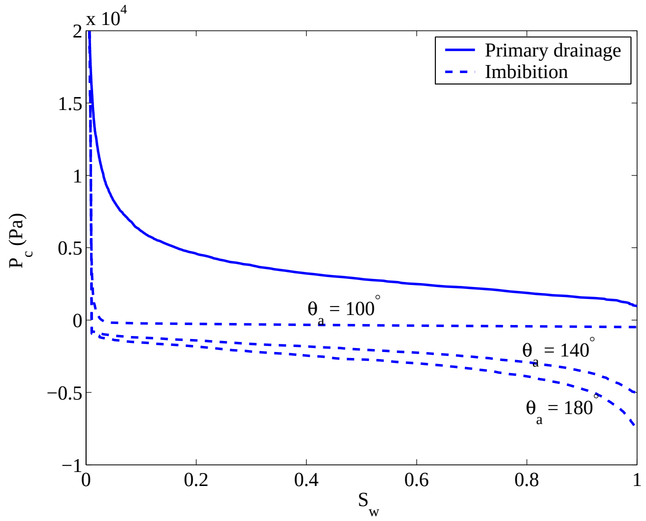

Figure 6: Imbibition curves for three different advancing contact angles: $\theta_a = 100°$, $\theta_a = 140°$ and $\theta_a = 180°$.

maximum.

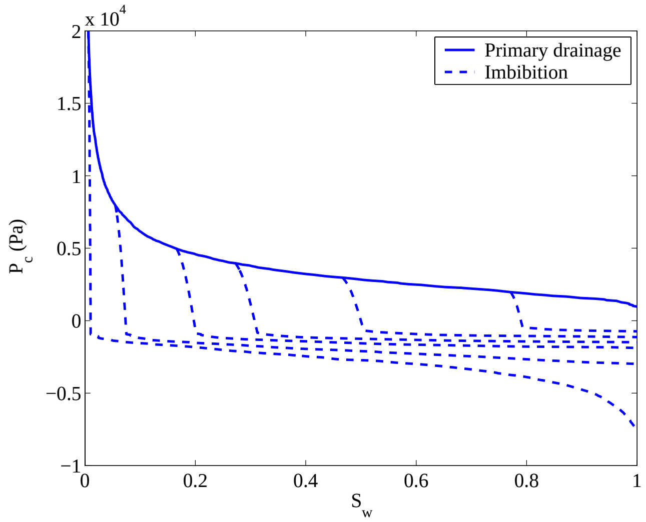

Figure 7: Imbibition curves from different reversal points on the primary drainage curve when $\theta_a = 180°$.

Fig. 8 shows the bounding hysteresis loop with a scanning loop inside assuming small contact angle hysteresis, with $\theta_a = 120°$ and $\theta_r = 100°$. Even though the contact angles indicate oilwet conditions and the P_c - curves are almost horizontal, the bounding loop includes spontaneous and forced invasion processes during both imbibition and secondary drainage in addition to smooth crossings at zero capillary pressure.

A bounding hysteresis loop with two scanning loops inside is presented in **Fig. 9** assuming large contact angle hysteresis with $\theta_a = 180°$ and $\theta_r = 70°$. The main imbibition process was terminated when $S_w = 1$, and hence the following secondary drainage process is a totally enforced invasion process from configuration D to C. However, the two drainage curves

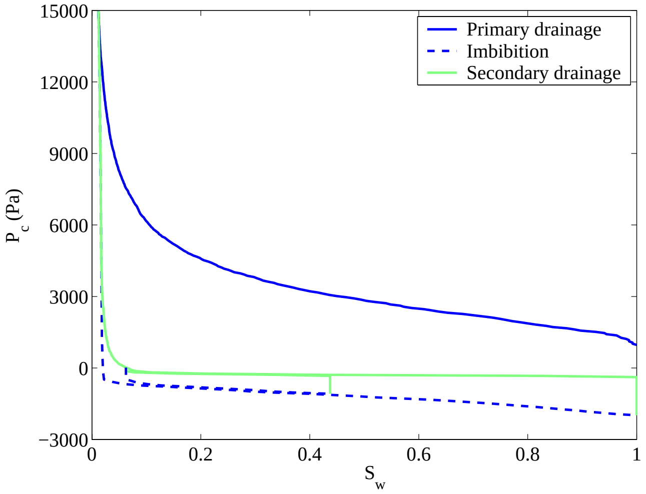

Figure 8: Bounding hysteresis loop with a scanning loop inside when $\theta_a = 120°$ and $\theta_r = 100°$.

originating from less negative $P_c^{\min}$ - values provide both spontaneous and forced displacements from configuration E to C since the oil layers tend to lower the capillary entry pressure. This leads to significantly lower capillary levels on the drainage scanning curves as compared to the bounding drainage curve, and hence the last scanning loop is entirely enclosed by the previous one. This effect is emphasized by the dependency of $P_c^{\min}$ on the entry pressure for tubes of configuration E, as illustrated in **Fig. 5**.

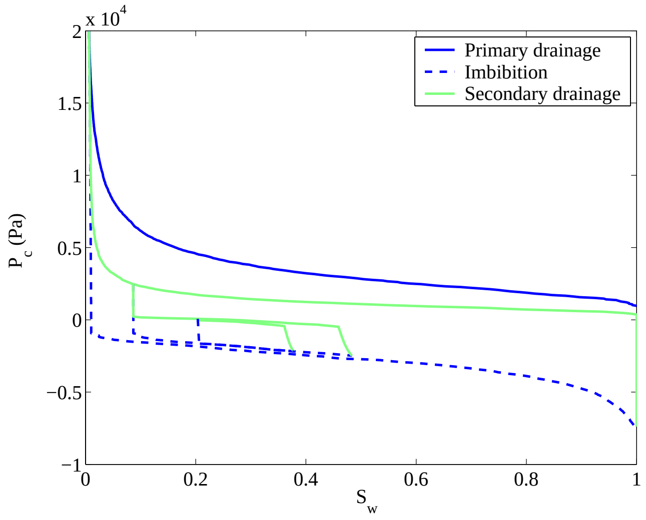

Figure 9: Bounding hysteresis loop with two scanning loops inside when $\theta_a = 180°$ and $\theta_r = 70°$.

So far we have only considered uniform contact angles during each of the drainage and imbibition processes. As a consequence, all possible displacements and observed generic trends are not included in the individual numerical experiments. Uniform contact angles provide capillary pressure curves with sharp corners and pronounced steps in the transitions between the different pore-scale events. The pore walls of real rock samples are composed of different mineralogical surfaces that have different affinity to crude oil. Hence, to reproduce realistic mixed-wet capillary pressure curves we assume that the advancing and receding contact angles are distributed. All the types of displacements and associated trends in capillary behavior may then be incorporated in a single simulation with different pore-scale events occuring within the same range of capillary pressure. This may result in smoother capillary pressure curves.

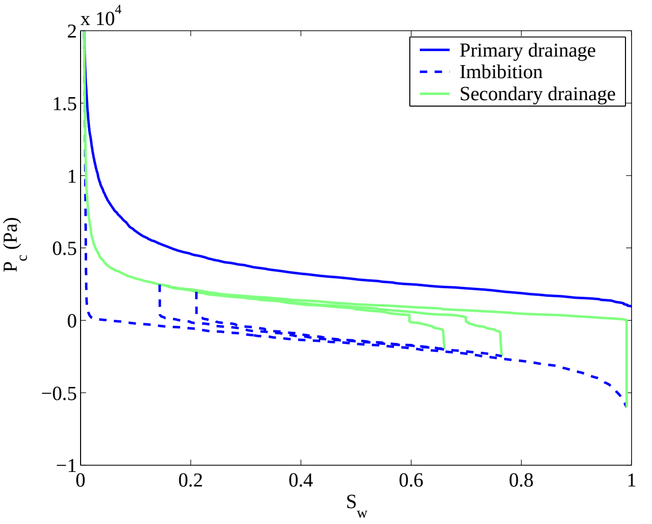

Figure 10: Bounding hysteresis loop with two scanning loops inside when θ_a is randomly distributed between 90° and 180° and $\theta_r = \theta_a/2$.

We consider randomly distributed $\theta_a \in [90°, 180°]$ and assume $\theta_r = \theta_a/2$. The bounding hysteresis loop with two scanning loops inside is presented in **Fig. 10**. The bounding imbibition curve was terminated at a capillary pressure where configuration C still existed in some of the tubes. At this point, oil layers were absent since all the displacements from configuration E to D had occured. Consequently, the subsequent bounding secondary drainage curve only includes forced displacements from configuration D to B and C. The other curves consitute segments of both spontaneous and forced processes, even though the selected contact angles indicate oilwet conditions in imbibition and waterwet conditions during secondary drainage. This is caused by the displacements from configuration C to D in imbibition and from configuration E to C in drainage, which both can occur at positive and negative capillary pressures for the selected set of contact angles. This demonstrates the applicability of the triangular tube model. The small steps on the two drainage scanning curves represent points where all tubes of configuration E has been invaded by oil. Further capillary pressure increments result in displacements from configuration D to C and B. The distributed contact angles also produce a spread of the oil-layer-invasion events during imbibition. To have crossings of zero capillary pressure located closer to each other, other contact angle distributions combined with smaller contact angle hysteresis may be assumed. To our knowledge, however, there is no experimental technique available to measure contact angle distributions for reservoir core samples.[25]

Correlation

Brooks and Corey[1] claimed that Eq. 1 only could be derived analytically if a uniform pore-size distribution was assumed. This implies a fixed pore-size distribution index, i.e., $a = 1/3$, and hence the flexibility of the correlation is reduced. We consider a more general distribution with the pore-size density

$$f_m(R) = \nu R_{\max}^{-\nu} R^{\nu-1}, \tag{48}$$

which includes the adjustable parameter $\nu > 0$. The uniform case corresponds to $\nu = 1$. The flexibility of Eq. 48 is demonstrated in **Fig. 11**. In some cases Eq. 48 may suffice as an approximation to pore-size distributions from core analysis.

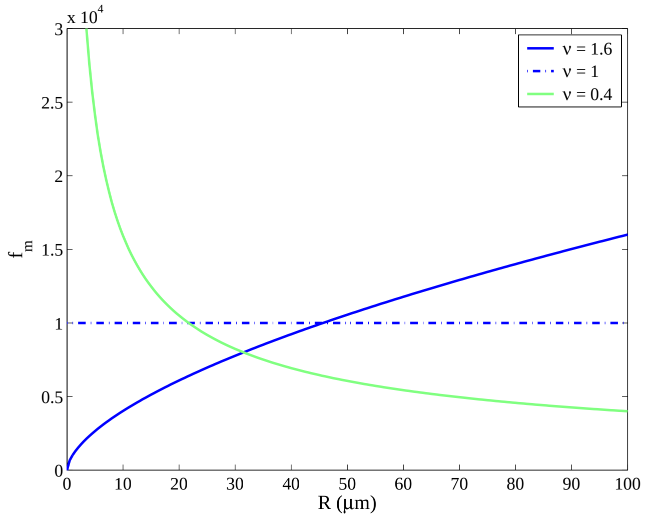

Figure 11: Pore-size density f_m as a function of R.

To derive a correlation for primary drainage based on Eq. 48 for the bundle-of-tubes model, we express the water saturation as a sum of two terms:

$$S_w = S_{wb} + S_{wc}, \tag{49}$$

where S_{wb} represents the contribution from the tubes completely filled with water, and S_{wc} is the contribution from the tubes with water residing in the corners after oil invasion. The saturations may be expressed as

$$S_{wb} = \frac{\int_0^{R_o} f_m A\, dR}{\int_0^{R_{\max}} f_m A\, dR}, \tag{50a}$$

$$S_{wc} = \frac{A_c \int_{R_o}^{R_{\max}} f_m\, dR}{\int_0^{R_{\max}} f_m A\, dR}, \tag{50b}$$

where R_o is the smallest pore size invaded by oil, and A is the cross-sectional area, Eq. 5. Notice that the area of water in the corners, A_c, is independent of pore size by Eq. 8. Furthermore, the capillary entry pressure is given by Eq. 9, and for the pore sizes $R_{\max}$ and R_o we denote the associated entry pressures by c and P_c, respectively. After some algebra Eqs. 49–50 yield

$$S_w = \left(\frac{c}{P_c}\right)^{\nu+2} + \epsilon\frac{\nu+2}{\nu}\left(\frac{c}{P_c}\right)^2\left[1-\left(\frac{c}{P_c}\right)^{\nu}\right], \quad . \quad . \quad . \quad (51)$$

where ϵ is a geometry factor given by

$$\epsilon = \frac{\cos\theta_{pd} - \sqrt{\frac{\tan\alpha}{2}(\sin 2\theta_{pd} - 2\theta_{pd} - 2\alpha + \pi)}}{\cos\theta_{pd} + \sqrt{\frac{\tan\alpha}{2}(\sin 2\theta_{pd} - 2\theta_{pd} - 2\alpha + \pi)}}. \quad . \quad (52)$$

The first term in Eq. 51 is the bulk saturation S_{wb}, and the second term is the corner saturation S_{wc}. Hence, for a bundle of triangular tubes, the Brooks–Corey expression is valid for the bulk saturation provided that the pore-size density is given by Eq. 48:

$$P_c = cS_{wb}^{-a}, \quad . \quad . \quad . \quad . \quad . \quad . \quad . \quad . \quad . \quad . \quad . \quad . \quad . \quad . \quad . \quad (53)$$

where the pore-size distribution index is related to ν by

$$a = \frac{1}{\nu+2}, \quad . \quad . \quad . \quad . \quad . \quad . \quad . \quad . \quad . \quad . \quad . \quad . \quad . \quad . \quad . \quad (54)$$

which implies $a < 1/2$. Eq. 53 may be inserted into Eq. 51 to provide an equation which relates S_{wb} to S_w:

$$S_w - S_{wb} - \epsilon\frac{\nu+2}{\nu}(S_{wb}^{\frac{2}{\nu+2}} - S_{wb}) = 0. \quad . \quad . \quad . \quad . \quad . \quad (55)$$

Notice that Eq. 53 reduces to Eq. 1 when $\epsilon = 0$. This corresponds to the special case when no water is residing in the corners after oil invasion, or to the idealized model of cylindrical pore shapes, i.e., when $S_w = S_{wb}$.

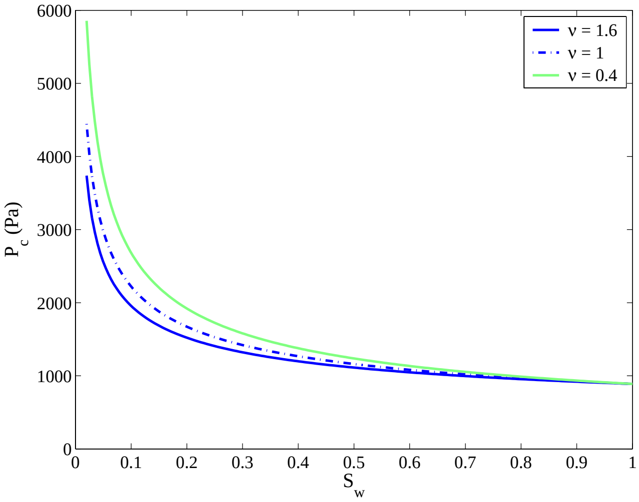

Figure 12: Capillary pressure curves for different parameters ν.

We have solved Eqs. 49, 53, 55 to study trends in capillary pressure and corner saturation for several values of ν. The results are shown in **Figs. 12**, **13**. An increased value of ν yields a decreased level of capillary pressure and an increased maximum corner saturation.

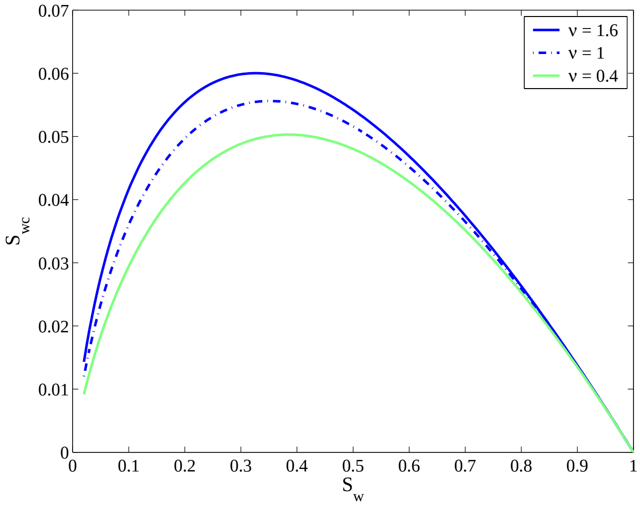

Figure 13: Corner saturation as a function of total water saturation for several values of ν.

We have not attempted to derive accurate algebraic expressions similar to Eqs. 53, 55 for imbibition and secondary drainage. All the pore-scale events and the capillary trends observed for different contact angles would complicate this approach and increase the number of parameters that have to be determined.

Rather than continue the analysis based on Eq. 48, we have chosen to compare the simulation model with the correlations given by Eqs. 1, 2, still assuming Weibull-distributed pore sizes obtained from Eq. 4. We consider randomly distributed $\theta_a \in [90°, 180°]$ with $\theta_r = 0.7\theta_a$ to ensure that the imbibition and secondary drainage curves both include segments representing spontaneous and forced displacements. The primary drainage curve is compared with Eq. 1, and the bounding imbibition and secondary drainage curves are compared with Eq. 2. A standard curvefitting method is employed to estimate the correlation parameters. For the imbibition and secondary drainage curves an initial water saturation S_{wi} is estimated in addition. The residual oil saturation is set to zero. The curvefitting procedure for the bounding curves is as follows: For small S_w only the first term in Eq. 2 is fitted to estimate c_w, a_w and S_{wi}. Similarly, the second term in Eq. 2 provide estimates for c_o and a_o when $S_o \to 0$. While the estimated S_{wi} is fixed, the parameters c_w, a_w, c_o and a_o are optimized simultaneously for the entire saturation range using both terms in Eq. 2. The results are presented in **Fig. 14**. The estimated parameters are as follows: $c = 1677.8$ Pa, $a = 0.6$ (primary drainage), $c_w = 22.8$ Pa, $a_w = 1.1$, $c_o = -1336.3$ Pa, $a_o = 0.4$, $S_{wi} = 0.005$ (imbibition), and $c_w = 55.2$ Pa, $a_w = 0.99$, $c_o = -189.1$ Pa, $a_o = 0.64$, $S_{wi} = 0.005$ (secondary drainage). The simulated curves agree fairly well with the correlation. A better match may, however, be obtained using appropriate error weighting. [2]

To describe three-phase transition zones and the dynamics of water-oil and gas-oil contact movements, a three-phase capillary pressure correlation is needed for mixed-wet reservoirs. We are currently extending the triangular tube model to simulate physically reasonable three-phase saturation paths. The

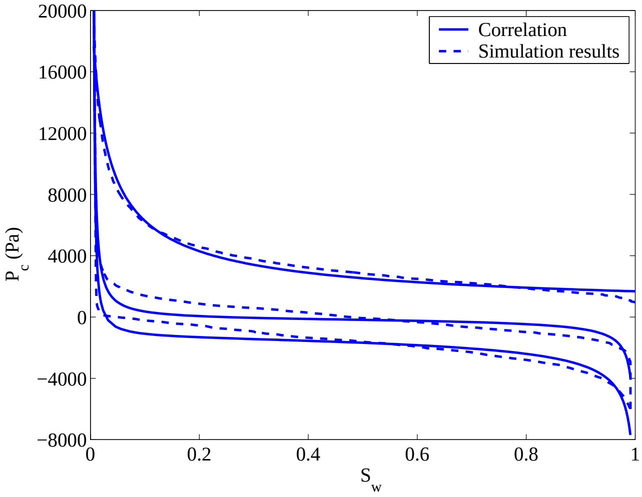

Figure 14: Primary drainage and bounding hysteresis loop from the simulation model with θ_a randomly distributed between 90° and 180° and $\theta_r = 0.7\theta_a$. The simulated data are compared with the correlations.

proven applicability range and the good match between the simulated results and Eqs. 1, 2 for two phases indicate that the model could also prove useful in the development of a three-phase correlation. Special attention is required for situations where one of the three phases appears or disappears, e.g., transitions between the gas and oil phase in condensate reservoirs, or when zero residual oil saturation is approached by drainage through connected layers. A correlation should be designed to account for a smooth transition between two- and three-phase flow.

Conclusions

1. A bundle-of-triangular-tubes model is developed to simulate mixed-wet capillary pressure curves with hysteretic scanning loops originating from any reversal point. The specific conclusions are:
    - Six different cross-sectional fluid configurations may occur for the sequence of processes primary drainage, imbibition and secondary drainage.
    - The effect of corner fluid occupancy on the capillary entry pressures is demonstrated: Waterfilled corners tend to increase the entry pressure, while oil layers tend to decrease the entry pressure.
    - The simulations demonstrate that the main characteristics of realistic mixed-wet capillary pressure curves may be reproduced by the model.
2. The Brooks–Corey correlation, Eq. 1, is valid for a bundle of triangular tubes when capillary pressure is correlated with the bulk saturation and the pore-size density is given by Eq. 48.
3. Results from the simulation model are compared with a correlation validated by experimental data, Eq.2. Work is in progress to investigate if Eq. 2 also suffices for a description of three-phase P_c - curves made by the model.

Nomenclature

a = Correlation parameter, see Eq. 1
A = Cross-sectional tube area
b = Position of arc meniscus
c = Correlation parameter, see Eq. 1
f = Probability density function
L = Cross-sectional length
P = Pressure
r = Radius of curvature
R = Radius of the inscribed circle
S = Saturation
x = Random number between 0 and 1
α = Corner half angle
β = Angle defined from geometry of the AMs in the corners, see Eq. 18
ϵ = Geometry factor, Eq. 52
η = Parameter in the Weibull distribution
θ = Contact angle
ν = Parameter in modified pore-size distribution
σ = Interfacial tension

Subscripts

a = Advancing
b = Bulk
c = Capillary or corner
ch = Characteristic
eff = Effective
f = Fluid
i = Initial
h = Hinging
imb = Imbibition
m = Modified
max = Maximum
min = Minimum
o = Oil
pd = Primary drainage
r = Receding
s = Solid
w = Water

Superscripts

crit = Critical
l = Layer
max = Maximum
min = Minimum

Abbreviations

AM = Arc meniscus
MS–P = Mayer and Stowe – Princen
MTM = Main terminal mensicus

Acknowledgements

Support for Johan Olav Helland was provided by Statoil through the VISTA program.

References

1. Brooks, R.H. and Corey, A.T.: "Hydraulic properties of porous media," Hydraulic paper no. 3, Colorado State University, 1964.
2. Skjaeveland, S.M., Siqveland, L.M., Kjosavik, A., Hammervold Thomas, W.L., and Virnovsky, G.A.: "Capillary pressure correlation for mixed-wet reservoirs," *SPERE* (2000) **3**, No. 1, 60–67.
3. Huang, D.D., Honarpour, M.M., and Al-Hussainy, R.: "An improved model for relative permeability and capillary pressure incorporating wettability," paper presented at the 1997 Society of Core Analysts International Symposium, Calgary, Sept. 7–10.
4. Princen, H.M.: "Capillary pressure behavior in pores with curved triangular cross-section: effect of wettability and pore size distribution," *Coll. Surf.* (1992) **65**, 221–230.
5. Kovscek, A.R., Wong, H., and Radke, C.J.: "A pore-level scenario for the development of mixed wettability in oil reservoirs," *Am. Inst. Chem. Eng. J.* (1993) **39**, No. 6, 1072–1085.
6. Blunt, M.J.: "Physically-based network modeling of multiphase flow in intermediate-wet porous media," *J. Pet. Sci. Eng.* (1998) **20**, 117–125.
7. Dong, M., Dullien, F.A.L., and Chatzis, I.: "Imbibition of oil in film form over water present in edges of capillaries with an angular cross section," *J. Coll. Int. Sci.* (1995) **172**, 21–36.
8. Keller, A.A., Blunt, M.J., and Roberts, P.V.: "Micromodel observation of the role of oil layers in three-phase flow," *Transport in Porous Media* (1997) **26**, 277–297.
9. Hui, M. and Blunt, M.J.: "Effects of wettability on three-phase flow in Porous Media," *J. Phys. Chem. B* (2000) **104**, 3833–3845.
10. Øren, P.E., Bakke, S., and Arntzen, O.J.: "Extending predictive capabilities to network models," *SPE Journal* (Dec. 1998) 324–336.
11. Singh, M. and Mohanty, K.K.: "Dynamic modeling of drainage through three-dimensional porous materials," *Chem. Eng. Sci.* (2003) **58**, 1–18.
12. Diaz, C.E., Chatzis, I., and Dullien, F.A.L.: "Simulation of capillary pressure curves using bond correlated site percolation on a simple cubic network," *Transport in Porous Media* (1987) **2**, 215–240.
13. Mayer, R.P. and Stowe, R.A.: "Mercury porosimetry – breakthrough pressure for penetration between packed spheres," *J. Coll. Sci.* (1965) **20**, 893–911.
14. Princen, H.M.: "Capillary phenomena in assemblies of parallel cylinders. I. Capillary rise between two cylinders," *J. Coll. Int. Sci.* (May 1969) **30**, No. 1, 69–75.
15. Princen, H.M.: "Capillary phenomena in assemblies of parallel cylinders. II. Capillary rise in systems with more than two cylinders," *J. Coll. Int. Sci.* (Jul. 1969) **30**, No. 3, 359–371.
16. Princen, H.M.: "Capillary phenomena in assemblies of parallel cylinders. III. Liquid columns between horizontal parallell cylinders," *J. Coll. Int. Sci.* (Oct. 1970) **34**, No. 2, 171–184.
17. Ma, S., Mason, G., and Morrow, N.R.: "Effect of contact angle on drainage and imbibition in regular polygonal tubes," *Coll. Surf. A: Phys. Eng. Asp.* (1996) **117**, 273–291.
18. Hirasaki, G.J.: "Wettability: Fundamentals and surface forces," *SPEFE* (June 1991) 217–225.
19. Morrow, N.R.: "The effects of surface roughness on contact angle with special reference to petroleum recovery," *J. Can. Pet. Tech.* (1975) **14**, No. 4, 42–53.
20. Yang, S.-Y., Hirasaki, G.J., Basu, S., and Vaidya, R.: "Mechanisms for contact angle hysteresis and advancing contact angles," *J. Pet. Sci. Eng.* (1999) **24**, 63–73.
21. Jerauld, G.R. and Rathmell, J.J.: "Wettability and relative permeability of Prudhoe Bay; a case study in mixed-wet reservoirs," *SPERE* (Feb. 1997) 58–65.
22. Patzek, T.W.: "Verification of a complete pore network simulator of drainage and imbibition," paper SPE 59312 presented at the 2000 SPE/DOE Improved Oil Recovery Symposium, Tulsa, Oklahoma, Apr. 3–5.
23. van Dijke, M.I.J. and Sorbie, K.S.: "Existence of fluid layers in the corners of a capillary with non-uniform wettability," *J. Coll. Int. Sci.* (2005) Article in press.
24. Helland, J.O.: *Modelling of three-phase capillary pressure for mixed-wet reservoirs*, PhD dissertation, University of Stavanger (2005) In press.
25. Dixit, A.B., McDougall, S.R., Sorbie, K.S., and Buckley, J.S.: "pore-scale modeling of wettability effects and their influence on oil recovery," *SPERE* (Feb. 1999) **2**, No. 1, 25–36.